Two-way quantum time transfer: a method for daytime space-Earth links

Randy Lafler,[1,*] Mark L. Eickhoff,[2] Scott C. Newey,[2] Yamil Nieves Gonzalez,[2] Kurt E. Stoltenberg,[2] J. Frank Camacho,[3] Mark A. Harris,[3] Denis W. Oesch,[3] Adrian J. Lewis,[1] and R. Nicholas Lanning[1]

[1] *Air Force Research Laboratory, Directed Energy Directorate, Kirtland AFB, New Mexico, United States*
[2] *The Boeing Company, Albuquerque, New Mexico, USA*
[3] *Leidos, Albuquerque, New Mexico, USA*

(Received 14 July 2023; revised 11 June 2024; accepted 12 July 2024; published 6 August 2024)

High-precision remote clock synchronization is crucial for many classical and quantum network applications. Evaluating options for space-Earth links, we find that traditional solutions may not produce the desired synchronization for low Earth orbits and unnecessarily complicate quantum networking architectures. Demonstrating an alternative, we use commercial off-the-shelf quantum photon sources and detection equipment to synchronize two remote clocks across our free-space testbed utilizing a method called two-way quantum time transfer (QTT). We reach picosecond-scale timing precision under very lossy and noisy channel conditions representative of daytime space-Earth links and software-emulated satellite motion. This work demonstrates how QTT is potentially relevant for daytime space-Earth quantum networking and/or providing high-precision timing in GPS-denied environments.

DOI: 10.1103/PhysRevApplied.22.024012

I. INTRODUCTION

Precise synchronization of remote clocks is important for position, navigation, and timing, high-speed transactions, distributed computing, quantum networking, and many other applications. One can synchronize remote clocks with global positioning system (GPS) public signals and achieve nanosecond-scale synchronization [1]. If more precision is desired, or one is operating in a GPS-denied environment, other techniques must be used. Perhaps the most straightforward optical-time-transfer technique uses pulsed lasers, photodetectors, and software-based correlation methods. For example, time transfer by laser link demonstrations have achieved picosecond-scale precision between remote ground stations operating in common view with the *Jason-2* satellite after a 1000-s acquisition [2]. Optical two-way time and frequency transfer (O-TWTFT) utilizes frequency combs to synchronize two remote clocks to femtosecond precision [3,4]. To date, demonstrations of O-TWTFT have been performed between stationary sites [3–5] and slow-moving drones with velocities below 25 m/s, but there are anticipated problems with the large Doppler shifts associated with low Earth orbits (LEOs) that have not been resolved [5]. Furthermore, femtosecond-scale synchronization based on O-TWTFT may be excessive for some applications and thus not justify the additional cost and complexity. Alternatively, the White Rabbit protocol can achieve picosecond-level precision and has been investigated for quantum networking synchronization [6–8]. It was designed for wireline fiber-optic applications but has been implemented wirelessly [9] and considered for space applications [10]. However, these techniques all introduce systems and hardware that may unnecessarily complicate quantum networking architectures.

A more direct and economical solution would utilize the femtosecond-scale temporal correlations of photon pairs that are already being exchanged for quantum communication tasks. In this case, the relative time offset between two remote clocks is measured with the following procedure: first, a series of photon pairs are separated and transmitted to two remote sites; second, the photons are detected and their arrival times are time-tagged based on the respective local clock; and third, after sufficient detection events are collected, the series of arrival times from each site are combined and correlation methods are used to find the clock offset. This technique was first proposed in Ref. [11] and we refer to it as quantum time transfer (QTT). One-way QTT enables relative clock synchronization [12], and two-way QTT enables absolute clock synchronization [13]. Subsequently, we investigated the suitability of this method for lossy and noisy channel conditions commensurate with long-fiber links and daytime space-Earth downlinks [14]. Others have investigated security [15], emulated free-space links in a lab setting [16], considered QTT for

*Contact author: AFRL.RDSS.OrgMailbox@us.af.mil

global-scale architectures [17,18], and implemented it in deployed fiber [19].

In this paper, we report remote clock synchronization and ranging with two-way QTT during atmospheric conditions representative of bidirectional Earth-satellite links and software-emulated satellite motion to $\mathcal{O}(1/c)$, that is, first-order Doppler effect [20]. Our system achieves picosecond-scale timing precision during these challenging conditions with commercial off-the-shelf hardware. We discuss the measured clock offset, the overlapping Allan deviation, the time deviation, the emulated satellite range, and the coincidence-to-accidental ratio (CAR) of the QTT correlation signals relative to the sky noise.

II. EXPERIMENTAL SETUP

A. Free-space channel

Our free-space quantum communication testbed is located at the Starfire Optical Range , Kirtland AFB, New Mexico, in the southwestern United States. The transceiver sites are the same sites utilized in Ref. [21], but are enhanced for two-way propagation using the arrangement in Fig. 1. The transceivers Alice and Bob represent satellite and ground station, respectively. We tune the Alice-to-Bob direction to be representative of a LEO downlink; we set the beam defocus to impose the correct geometric loss, we use a white light source to scatter noise photons into the channel, we use a heat source to add scintillation, and we utilize a closed-loop adaptive optics (AO) system to monitor and compensate for atmospheric turbulence [21].

Atmospheric turbulence causes spatial decoherence at the entrance pupil of the optical receiver. In the focal plane, the reduced constructive interference results in a broadened and chaotic signal; see the intensity distribution in Fig. 2(a). Higher-order AO corrects for spatial decoherence in the pupil plane and restores constructive interference in the focal plane; see the nearly diffraction limited Airy pattern in Fig. 2(b). The quantum signal is focused through a 40-μm circular field stop (FS), which serves as a spatial filter to reject sky-noise photons; see the red circles in Figs. 2(a) and 2(b). The 40-μm FS restricts the quantum channel field-of-view to the roughly 5.6-μrad diffraction-limited field of view and permits the use of a broad 10-nm spectral filter. Thus, Fig. 2(b) illustrates how the AO system permits spatial filtering at the diffraction limit while maintaining quantum signal throughput. It is this technique that enables daytime operation [21].

In the "downlink" direction we introduce defocus to create 11 dB of geometric loss commensurate with a 700-km link using a 20-cm transmitter and a 1-m receiver. Other constant loss comes from the receive-telescope optics $\eta_{\text{rec}} \approx 0.5$, the spectral filter $\eta_{\text{spec}} \approx 0.9$, the detectors $\eta_{\text{det}} \approx 0.6$, and the spatial filter $\eta_{\text{FS}} \approx 0.84$ [21]. Altogether, the loss associated with the experimental arrangement is about 17 dB. The remainder of the loss

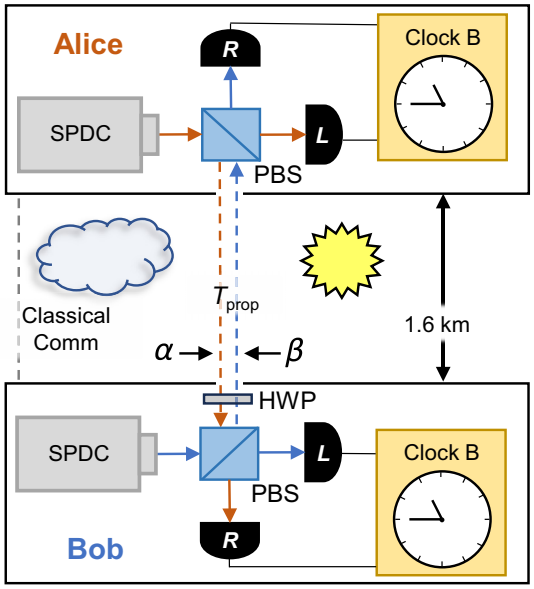

FIG. 1. Schematic of two-way quantum time transfer (QTT) field experiment. Each site is equipped with a spontaneous parametric down-conversion (SPDC) biphoton source, local L and receive R detectors, and a local clock consisting of a time tagger, a rubidium frequency standard, and a PC. The sites are separated by a 1.6-km free-space channel with propagation time T_{prop}. The "downlink" direction α and "uplink" direction β represent the directions for the emulated satellite pass. The classical channel is utilized for sharing time tags. PBS, polarizing beam splitter; HWP, half wave plate.

observed comes from the fluctuating atmospheric scattering and absorption and the loss at the spatial filter due to imperfect AO correction. Figure 2(c) gives the histograms of the channel attenuation for the downlink (red line) and uplink (blue line) directions with the higher-order AO in the open- (dashed line) and closed-loop (solid line) configurations. It shows that the average channel attenuation with and without higher-order AO in the downlink direction is approximately 26 dB and 41 dB, respectively.

In the Bob-to-Alice "uplink" direction, the quantum signal was precompensated by the AO system, and photons arrived at Alice with slightly better efficiency than the downlink direction due to less divergence; see the solid blue line in Fig. 2(c). We apply an additional 2 dB of attenuation to the true coincidences in the receive channel at the Alice site in order to make our "uplink" direction attenuation the same as the "downlink" direction. This level of attenuation corresponds to AO compensation with a beacon in the point-ahead direction [22]. See Appendix E for more details of the performance of QTT with more channel attenuation and quantum signal fades.

B. Two-way QTT

Figure 1 gives a schematic of the two-way QTT components. The sites labeled Alice and Bob each have a Thor Labs SPDC810 biphoton source and a pair of

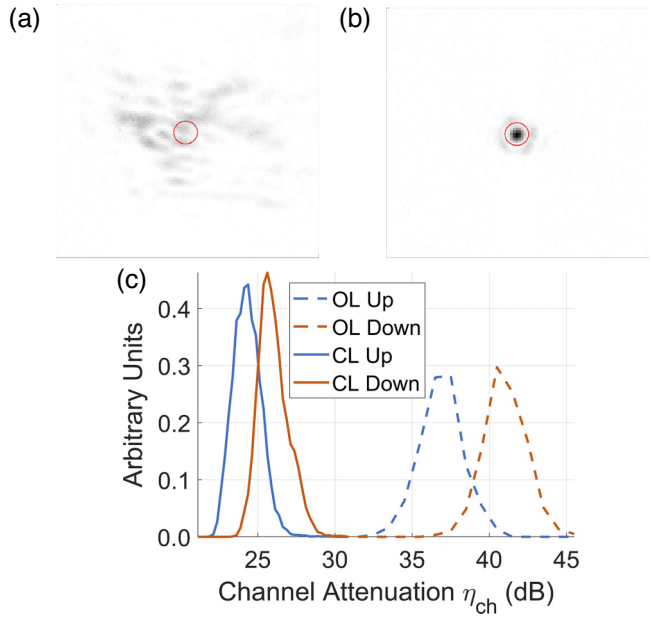

FIG. 2. Example scoring camera frames (a) without and (b) with higher-order adaptive optics (AO). The scoring camera takes focal-plane images of the AO laser beacon and is optically conjugate to the quantum path. Thus, the distributions in (a,b) correspond to the probability distribution of the quantum signal photon and the red circle represents the size of the 40-μm field stop (FS) used for spatial filtering sky-noise photons. In (c), the channel attenuation histograms are plotted for the α "downlink" (red line) and β "uplink" (blue line) directions when the higher-order AO is in the closed-loop (solid line) and open-loop (dashed line) configurations.

Excelitas SPCM-AQRH detectors labeled L and R for local and receive, respectively, paired with 10-nm spectral filters. The clock system is comprised of a PC, a Picoquant Hydraharp 400 time tagger, and a Stanford Research Systems FS725 rubidium frequency standard , which uses the PRS10 rubidium oscillator. Alice and Bob each randomly create a pair of photons, detect one of the pair with their local detector L, and send the other photon across the 1.6-km free-space channel to the other site where it is detected with a receive detector R. Later we will emulate satellite motion in the field experiment data, so we write the detection times t in the "downlink" direction α and "uplink" direction β as

$$\begin{aligned} t_{B,R} &= t_{A,L} + T^{(\alpha)}_{\text{prop}}(t_{A,L}) + \delta, \\ t_{A,R} &= t_{B,L} + T^{(\beta)}_{\text{prop}}(t_{B,L}) - \delta, \end{aligned} \tag{1}$$

where the subscripts A and B correspond to the local clocks at Alice and Bob, respectively, $T^{(i)}_{\text{prop}}$ are the directionally dependent propagation times, and δ is the absolute clock offset where we make the approximation $\delta = \delta^{(\alpha)} = \delta^{(\beta)}$. Rearranging Eq. (1), one can define the relative clock offsets τ_α and τ_β:

$$\begin{aligned} \tau_\alpha &= t_{B,R} - t_{A,L} = T^{(\alpha)}_{\text{prop}}(t_{A,L}) + \delta, \\ \tau_\beta &= t_{A,R} - t_{B,L} = T^{(\beta)}_{\text{prop}}(t_{B,L}) - \delta. \end{aligned} \tag{2}$$

Combining Eqs. (2), we find the absolute clock offset [13]

$$\delta = \frac{1}{2}\left(\tau_\alpha - \tau_\beta - T^{(\alpha)}_{\text{prop}}(t_{A,L}) + T^{(\beta)}_{\text{prop}}(t_{B,L})\right). \tag{3}$$

C. Measured channel conditions

In our field experiment we performed two-way QTT over a range of atmospheric conditions. In Fig. 3(a) we show the measured turbulence parameters [r_0, σ_I^2], where each data point represents a 1-second average. The projections onto the Hufnagel Valley 1×, 2×, and 3 × $HV_{5/7}$ theoretical turbulence profiles [21] show that the atmospheric conditions were similar to or worse than an Earth-satellite downlink. For further analysis, we select two continuous 1-hr data sets from the total data (gray) that are representative of daytime (blue) and nighttime (black) atmospheric conditions. The average true coincidence rate for the two conditions and two directions is roughly 1000 cps. Figure 3(b) shows the CAR of the QTT correlation signal in the α direction as a function of the background sky radiance H_b measured during the daytime scenario; this indicates that the QTT algorithm reliably finds the true correlation signal with a bright sky background even as the CAR approaches 1. To account for Earth albedo and scattering [23] in the uplink channel, we add noise to the receive detector data stream [14] corresponding to 23 W/(m^2 sr μm) using the expression for the number of noise photons with a diffraction-limited field of view $N_{b\,\text{DL}}$ in Ref. [21].

III. QTT ANALYSIS

A. Stationary analysis

For our initial analysis, we consider the timing performance of our two-way QTT clock system in the stationary field experiment. We do this by utilizing the following two logical or "software" clocks. One is drifting, that is, the frequency standards drift apart and the absolute clock offset δ is simply tracked. For the synchronized clock we perform the following recursive algorithm where the acquisition time $T_a = 1$ s [14]: for the ith acquisition we estimate the fractional-frequency drift $\Delta U_j^{(i)} = (\tau_j^{(i)} - \tau_j^{(0)})/T_a$ in each direction j, we shift the new received time tags according to $t_j^{(i+1)} + \Delta U_j^{(i)}\, T_a$, perform the QTT correlations, then use Eq. (3) to find the absolute offset $\delta^{(i+1)}$.

The results are shown in Fig. 3(c) for the daytime and nighttime scenarios with the synchronized (solid curves and left axis) and drifting (dashed curves and right axis) clocks. The standard deviations are 27.1 and 39.7 ps

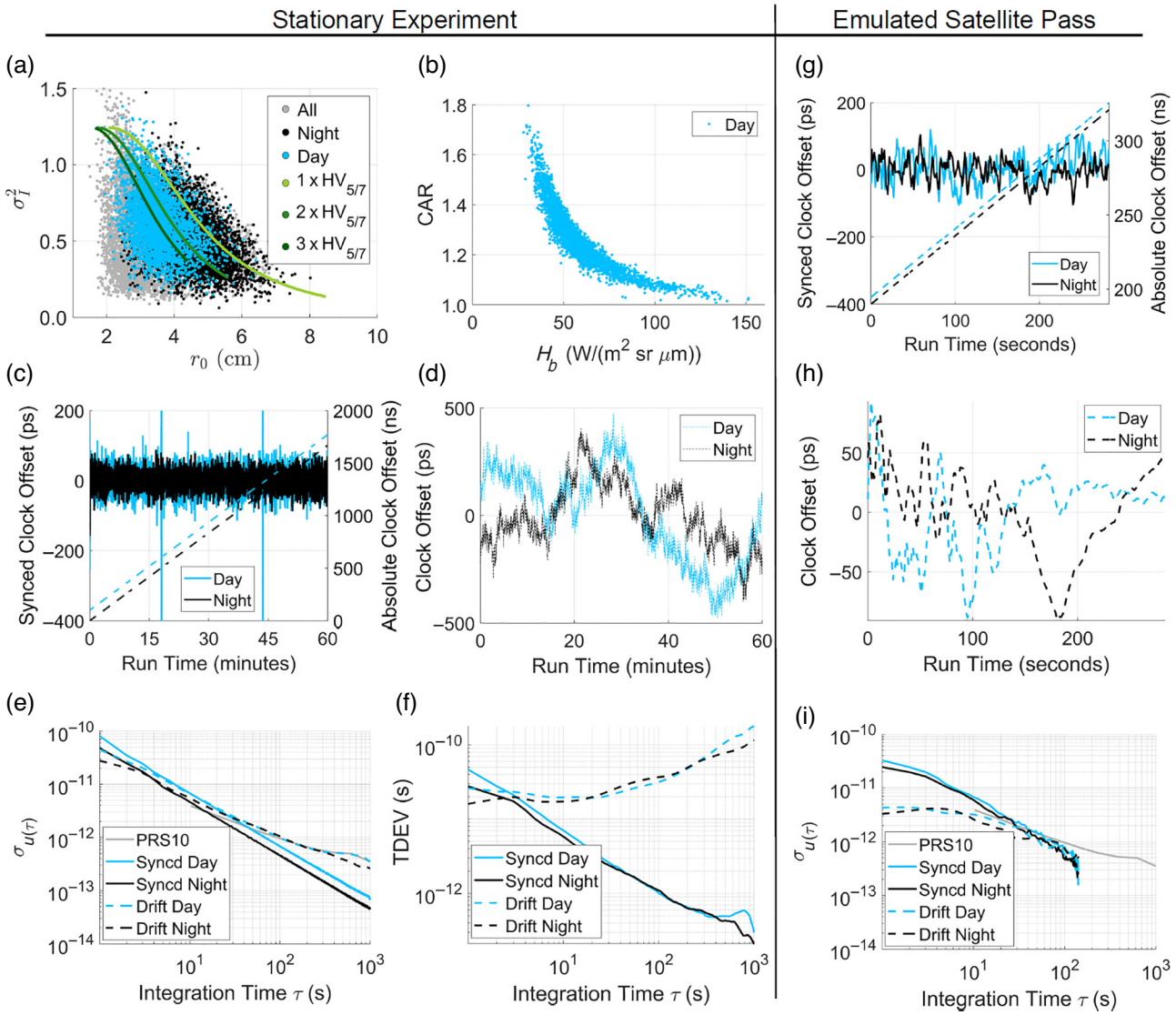

FIG. 3. (a) The measured turbulence parameters $[r_0, \sigma_I^2]$ and their projections onto the $1\times$, $2\times$, and $3 \times HV_{5/7}$ turbulence profiles [21]. The representative 1-hr acquisitions under daytime and nighttime conditions are in blue and black, respectively. All other data is shown in gray. (b) The coincidence-to-accidental ratio as a function of the background sky radiance H_b for the daytime scenario. (c) The absolute offset of the synchronized clock (solid curves and left axis) and the drifting clock (dashed curves and right axis). In (d) we take the drifting clock offset measurements and remove the linear trend to reveal the fluctuations in picoseconds. In (e,f) we plot the overlapping Allan deviation and time deviation measured by the synchronized (solid) and drifting (dashed) clocks, respectively. The gray line is the Allan deviation quoted in the Stanford Research Systems PRS10 manual. In (g)–(i) we present analogous plots for an emulated satellite pass.

for the nighttime and daytime scenarios, respectively. As expected, the timing jitter is smaller at night. Meanwhile, the drifting clock shows that the local clocks drift from each other at a rate of about 450 ps per second on average. Figure 3(d) shows the absolute clock offset δ according to the drifting clock after the mean clock drift is removed; this reveals the jitter of the QTT system, which is a consequence of the hardware components and atmospheric effects. Altogether, we see that the two-way QTT algorithm can run continuously without losing synchronization for an extended period of time under challenging channel conditions.

The Allan deviation is a standard method to characterize the stability and noise profile of a clock system [24]. In Fig. 3(e) we show the overlapping Allan deviation, where the solid and dashed curves are the synchronized and drifting clocks, and the daytime and nighttime scenarios are blue and black, respectively. The gray curve is the Allan deviation reported in the user manual of the Stanford Research Systems PRS10. The slopes for

the drifting and synchronized clocks are approximately -0.6 and -1, respectively. In Fig. 3(f) we show the time deviations (TDEV) [24], which have slopes approximately $+1/2$ and $-1/2$ for the drifting and synchronized clocks, respectively. Combined, these results indicate that the predominate noise is white FM and white PM for the drifting and synchronized clocks, respectively. Visually, one can see these different noise profiles by comparing Figs. 3(c) and 3(d).

B. Analysis with motion

Since the Alice and Bob sites are stationary, we emulate relative motion by shifting the received time tags commensurate with a 700-km circular sun-synchronous orbit passing overhead from -30° to 30° elevation. This induces a large apparent frequency drift that broadens the QTT correlation signal [14]. If the coincidence rate is large enough, one can simply reduce the acquisition time to narrow the correlation signal and run the conventional QTT algorithm [14,17,18]. However, for our proof-of-principle demonstration, the coincidence rates are not sufficiently high. Consequently, we create an orbit tracking algorithm by parameterizing the orbit equation into a fitting function and use an iterative process to find the orbit altitude a, inclination θ_i, fractional frequency drift ΔU, and clock offset δ (see Appendixes C and D for more details). Figures 3(g)–3(i) show the analogous plots for the emulated satellite pass. Removing the effect of relative motion recovers the QTT coincidence signal and constitutes the drifting logical clock [see dashed line in Fig. 3(g)]. Removing the clock drift ΔU as well constitutes the synchronized logical clock [see Fig. 3(g) solid line]. The standard deviations of the synchronized clock are 43.2 and 46.9 ps for the nighttime and daytime scenarios, respectively. Figure 3(i) shows the noise profile as a consequence of the orbit tracking algorithm. In Fig. 4 we plot the slant range for the entire pass in the downlink direction. The gray points are the range of the emulated satellite orbit and the black (blue) lines are the measured range for the nighttime (daytime) conditions. The left axis gives the range in kilometers and the right axis gives the difference between the measured range d_{fit} and the emulated range d_{orbit}, which shows that the tracking algorithm has centimeter-scale precision and accuracy.

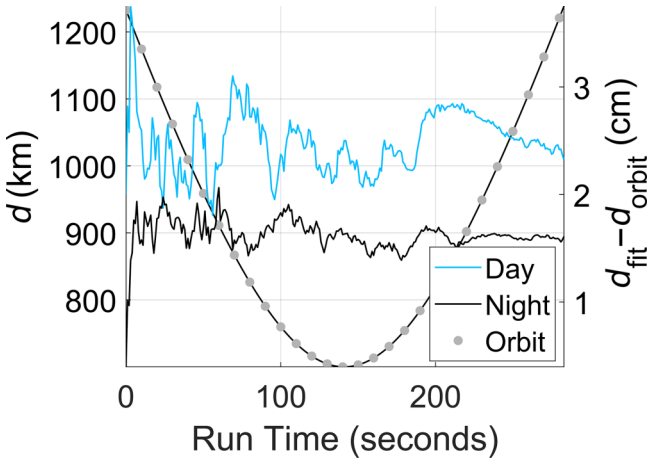

FIG. 4. Satellite range d versus run time for the emulated satellite pass in the downlink direction. The left axis and gray points show the emulated range and the intersecting lines are the measured range for the daytime and nighttime conditions. The right axis is the difference between the measured range d_{fit} and the emulated range d_{orbit} showing centimeter-scale fluctuations.

IV. CONCLUSION

In this paper we report a remote clock synchronization and ranging field experiment over daytime space-Earth channel conditions utilizing a protocol we call two-way quantum time transfer. Our algorithm synchronizes to tens of picoseconds after only 1 s of integration with modest photon sources and detection equipment. We analyze the performance of the protocol using the Allan and time deviations with synchronized and drifting software clocks. We establish the relevance to space-Earth links using a software-emulated low Earth orbit satellite pass to $\mathcal{O}(1/c)$. This work demonstrates a practical way to establish synchronization over a quantum link without unnecessarily complicating the system with extraneous time transfer methods. Follow-on research should include smaller relativistic effects to $\mathcal{O}(1/c^3)$, further optimization of the orbit-tracking algorithm, and modeling of more complicated tasks such as entanglement swapping.

ACKNOWLEDGMENTS

The authors acknowledge program management support from Valerie Knight, Jacob DeLange, Ryan Riley, and Ian Blake AFRL. The views expressed are those of the authors and do not necessarily reflect the official policy or position of the Department of the Air Force, the Department of Defense, or the U.S. government. The appearance of external hyperlinks does not constitute endorsement by the U.S. Department of Defense (DoD) of the linked websites, or the information, products, or services contained therein. The DoD does not exercise any editorial, security, or other control over the information you may find at these locations.

DISTRIBUTION A: Approved for public release; distribution is unlimited. Public Affairs release approval AFRL-2024-3082.

APPENDIX A: RELATIVE MOTION

Relative motion is a challenge for any time transfer system. Keeping time between a ground station and a satellite in LEO is complicated by a large first-order

Doppler shift $\mathcal{O}(1/c)$ and smaller relativistic effects [20]. We studied how the QTT algorithm performs when the clock drift is small with respect to the QTT correlation signal [14]. In this case, clock drifts $\Delta U \sim 10^{-10}$ do not significantly affect the QTT correlation signal [see Eq. (A7) in Ref. [14]]. Relativistic effects fall into this category and can be readily tracked by the standard QTT algorithm to picosecond-level precision. In the current analysis, it is important to show how the QTT algorithm performs with large first-order Doppler shifts that induce much larger clock drifts $\Delta U \sim 10^{-5}$.

In the 1.6-km testbed, traceability to daytime slant-path channels was achieved by rigorously characterizing and tuning the atmospheric turbulence and radiance conditions in the channel to match those of daytime slant-path propagation from space [21]. We also introduced beam defocus to create 11 dB of aperture coupling loss representative of diffraction effects over a propagation distance of 700 km. Thus, for this experiment, we emulate a 700-km circular sun-synchronous orbit with an inclination θ_i of 98.2°.

APPENDIX B: SYSTEM JITTER

In Fig. 5 we plot the range of the terrestrial testbed field experiment for the nighttime and daytime one-hour acquisitions. We use $d = c \times T_{\text{prop}}$, where $T_{\text{prop}} = (\tau_\alpha + \tau_\beta)/2$ is calculated using the relative offsets τ from the drifting clock. We find that the mean of both distributions is $\mu = 1.6445$ km with standard deviation of approximately 0.9 cm for the daytime and nighttime scenarios. The observed jitter is mainly due to the atmosphere and the detection equipment since the noise from the frequency standards tends to cancel due to the symmetry of the two-way protocol. On the other hand, when T_{prop} is calculated with respect to the synchronized clock, the noise is mostly white noise, which suggests that the system jitter is partially corrected for when ΔU is measured and applied in the predict-ahead algorithm. Therefore, the latter method could be used to enhance the measurement of T_{prop} and thus the range d. Nevertheless, we simply take the data and subtract the mean propagation time observed in the testbed before emulating motion. Therefore, all the jitter of the terrestrial field experiment, including the frequency standard jitter, is present in the emulated satellite pass.

APPENDIX C: EMULATING SATELLITE MOTION

We introduce the first-order Doppler effect by shifting Alice's and Bob's receiver time tags according to the propagation time

$$T_{\text{prop}} = d/c, \tag{C1}$$

where c is the speed of light and the slant range d is [25]

$$d = \sqrt{r^2 + R_E^2 - 2rR_E \cos\beta}, \tag{C2}$$

R_E is the Earth's radius, a is the altitude, $r \equiv R_E + a$, and β is the geocentric angle between the quantum ground station (QGS) and the satellite. From spherical trigonometry

$$\cos\beta = \cos\alpha\cos\gamma + \sin\alpha\sin\gamma\cos B, \tag{C3}$$

where the central angles are related to the latitudes λ,

$$\begin{aligned} \alpha &= \pi/2 - \lambda_{\text{SSP}}, \\ \gamma &= \pi/2 - \lambda_{\text{QGS}}, \end{aligned} \tag{C4}$$

the outer angle B is related to the longitudes ϕ,

$$B = \phi_{\text{QGS}} - \phi_{\text{SSP}}, \tag{C5}$$

and SSP stands for subsatellite point [see Fig. 6(a)].

To find the slant range d as a function of time we need the latitude and longitude of the satellite as functions of

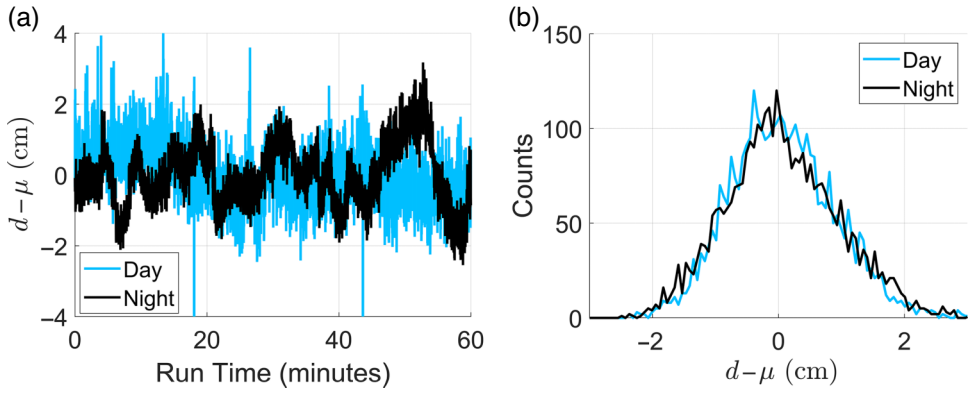

FIG. 5. Difference between the measured terrestrial testbed range d and the mean range $\mu = 1.6445$ km for the daytime (blue) and nighttime (black) scenarios. In (a) we give the range as a function of time and in (b) we give a histogram of the one-hour data acquisitions. The standard deviation is approximately 0.9 cm for both scenarios.

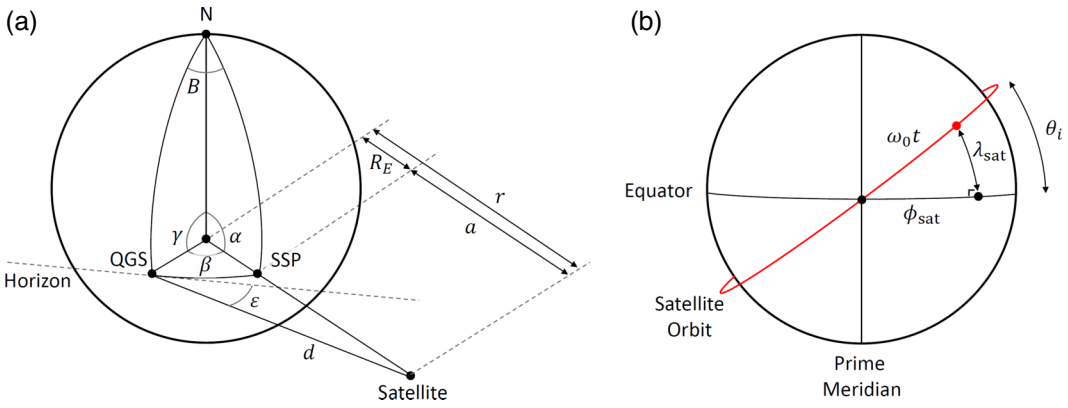

FIG. 6. (a) Graphic relating the geocentric angle β to the elevation angle ε and the slant range d. On the surface of the Earth there is a spherical geometry relating β to the central angles α and γ, which are functions of the latitudes λ, and the outer angle B, which is a function of the longitudes ϕ [see Eqs. (C4) and (C5)]. The two geometries are defined in terms of the north pole N, the location of the quantum ground station QGS, the satellite location, and the subsatellite point SSP. (b) Graphic of a spherical right triangle relating the latitude λ_{sat}, longitude ϕ_{sat}, and geocentric angle $\omega_0 t$ for a circular orbit of inclination θ_i.

time. Using Napier's rules for spherical right triangles [see Fig. 6(b)], we have

$$\begin{aligned} \sin\lambda_{sat}(t) &= \sin\omega_0 t \sin\theta_i, \\ \tan\phi_{sat}(t) &= \tan\omega_0 t \cos\theta_i. \end{aligned} \tag{C6}$$

Thus, for the latitude we find

$$\begin{aligned} \lambda_{sat}(t) &= \arcsin\left[\sin(\omega_0 t + \Lambda_0)\sin\theta_i\right], \\ \Lambda_0 &= \arcsin\left[\sin\lambda_{sat,0}/\sin\theta_i\right], \\ \omega_0 &= \sqrt{GM/r^3}, \end{aligned} \tag{C7}$$

where $\lambda_{sat,0}$ is the initial latitude, θ_i is the inclination angle, Λ_0 is a phase shift setting the initial satellite latitude when $t = 0$, G is the gravitational constant, and M is the mass of the Earth. The longitude is

$$\begin{aligned} \phi_{sat}(t) &= \arctan\left[\tan(\omega_0 t + \Lambda_0)\cos\theta_i\right] + \phi_{shift} + \phi_P, \\ \phi_{shift} &= \phi_{sat,0} - \arctan\left[\tan\Lambda_0 \cos\theta_i\right], \\ \phi_P &= (\omega_p - \omega_E)t, \end{aligned} \tag{C8}$$

where $\phi_{sat,0}$ is the initial longitude, ϕ_{shift} sets the initial longitude ($t = 0$) by correcting for the longitudinal shift induced by the phase shift Λ_0, ω_E is the angular velocity of the Earth's rotation, ω_p is the sun-synchronous precession, and ϕ_P is a shift due to the Earth's rotation and the satellite orbit precession. For our simulation, we set the initial satellite latitude and longitude to the ground station location so that the satellite is overhead at $t = 0$.

The uplink quantum signal must be pointed ahead of the downlink signal in order to intercept the satellite as it moves. We use the point-ahead approximation

$$\theta_{PA} = \frac{2}{c}\left(\frac{GM}{r}\right)^{1/2}\sin\varepsilon. \tag{C9}$$

This expression can be written as a function of time by solving $d\sin\varepsilon = r\cos\beta - R_E$ for ε and substituting $\cos\beta$ from Eq. (C3). Consequently, the propagation time is asymmetric; T_{prop} is different in the uplink and downlink directions.

APPENDIX D: REMOVING SATELLITE MOTION

1. Coarse orbit estimation

For a LEO satellite, the rate of relative motion during our 1-second acquisition time prohibitively broadens the roughly 1000 cps coincidence signal and makes it impossible to perform standard QTT [14] without precompensation. Thus, the first step of our algorithm is to take the uplink and downlink directions and perform a coarse scan over altitude a and inclination θ_i with a sufficiently large parameter space. For each a and θ_i, the corresponding $T_{prop}(t, a, \theta_i)$ is calculated and subtracted from the received time tags, QTT is performed, and the correlation signal peak height is recorded. The result is an island of acceptable parameters where the correlation peak is large and the compensation is accurate enough to isolate the coincidences. For example, Fig. 7 shows the parameter scan for the nighttime downlink scenario. Each red cell corresponds to an orbit-parameter pair $[a, \theta_i]$ that permits QTT to find the coincidences and move to the next step, despite the ambiguity with respect to the orbit.

2. Precise orbit estimation

Next, we take the coincidences found in the previous step and shift the received time tags back to their

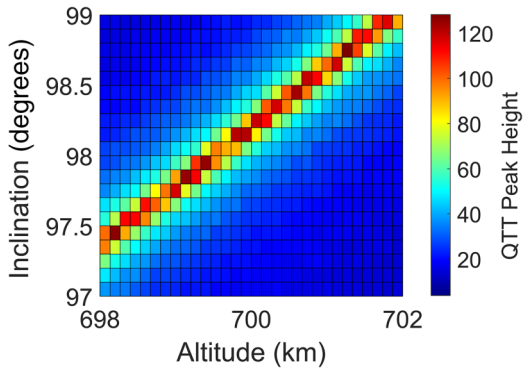

FIG. 7. Coarse search over the orbit inclination and altitude parameters. The color legend gives the QTT correlation peak height. The step sizes are 0.1° and 133 m, respectively.

uncompensated locations. We know that the time difference between coincident detection events is dominated by the Earth-satellite propagation time, but there is also the small linear clock drift inherent to the two Stanford Research Systems FS725 frequency standards. Thus, we take the time difference between coincident time tags τ and fit them with

$$\tau_{\text{fit}} \equiv T_{\text{prop}}(t, a, \theta_i) + m\,t + b, \tag{D1}$$

where the fit parameter m accounts for the fractional frequency drift ΔU and b accounts for the small vertical shift. This fit results in a more precise measurement of the orbit parameters a and θ_i as well as the frequency drift ΔU; thus the coarse orbit determination only needs to be performed once at the beginning of the pass. We perform the fit for the uplink and downlink directions, where the uplink T_{prop} also includes the point-ahead term in Eq. (C9).

3. Software clocks

The following recursive algorithm constitutes the synchronized clock: for each successive acquisition, the uplink and downlink τ_{fit} are used to remove the spreading of the time tags and the clock offset, and QTT is performed to measure the residual clock offset, isolate the new coincidences, add them to the prior coincidences, and update the fit. The drifting clock follows from the same fit, except that only the orbit components are removed; thus the clocks drift apart according to the fractional frequency drift ΔU. In the next subsection we show how the algorithm converges to the input altitude, inclination, and the drift between the frequency standards.

4. Algorithm performance

Figures 8(a)–8(c) show how the fit algorithm converges to the orbit altitude a, inclination θ_i, and fractional frequency drift ΔU, where the uplink and downlink fit parameters are dashed and solid, respectively. Figures 8(a) and 8(b) show that the fit parameters a_{fit} and θ_{fit} slowly converge to the input parameters a_{orbit} and θ_{orbit}. Figure 8(c) shows the uplink and downlink ΔU_{fit} converging to the clock drift of the Rubidium frequency standards in about the same time. The uplink and downlink orbit-fit parameters are mirror images of each other due to the interplay with the residual fractional frequency drift after removing τ_{fit}. For the downlink direction, the residual fractional frequency drift is positive and partially counteracting the effect of relative motion; this causes the fit to overestimate the altitude. The opposite is true for the uplink direction. Considering the nighttime case in Figs. 8(a)–8(c), one can see that after the satellite passes overhead and enough coincidences are collected, near t=200 s, the fitting algorithm can distinguish the two independent phenomenon and converges to the correct values. The daytime case converges slower due to a noisier coincidence signal.

Figures 8(d)–8(e) give the Allen deviation, modified Allen deviation, and time deviation, respectively. Comparing these results to the corresponding figures in the main text, one can see that the synchronized clocks perform similarly to the drifting clocks in the stationary scenario. The slope of the modified Allan deviation [Fig. 8(e)] is approximately -1, which indicates flicker PM noise, whereas the stationary synchronized clocks have white PM noise [24]. We suspect that the noise profiles are different due to the time it takes for the fit parameters to converge to the emulated orbit parameters. In other words, if the tracking algorithm was further optimized or if the satellite pass were longer, we suspect the slope of the modified Allen deviation would change to -1.5 and indicate white PM noise. This also explains why the drifting clocks are worse than the stationary scenario.

APPENDIX E: QTT UPLINK PERFORMANCE WITH MORE ATTENUATION

In Earth-satellite uplinks, the quantum signal is transmitted at a point-ahead angle so that it intercepts the LEO satellite. As a consequence, the uplink quantum signal travels a different path than the downlink quantum signal. Depending on the path of the AO beacon, this can result in additional loss due to reduced compensation of atmospheric-turbulence effects caused by anisoplanatism [26,27]. Performing the uplink with the AO loop closed on a *downlink* beacon would result in about 10 dB more attenuation [22], but when applying this level of attenuation we observe occasional loss of signal due to the relatively low-performance sources in this field experiment. However, the satellite tracking algorithm can maintain synchronization despite the occasional signal fade.

To demonstrate the resilience to signal fades, we present the performance of QTT for a nighttime uplink in which

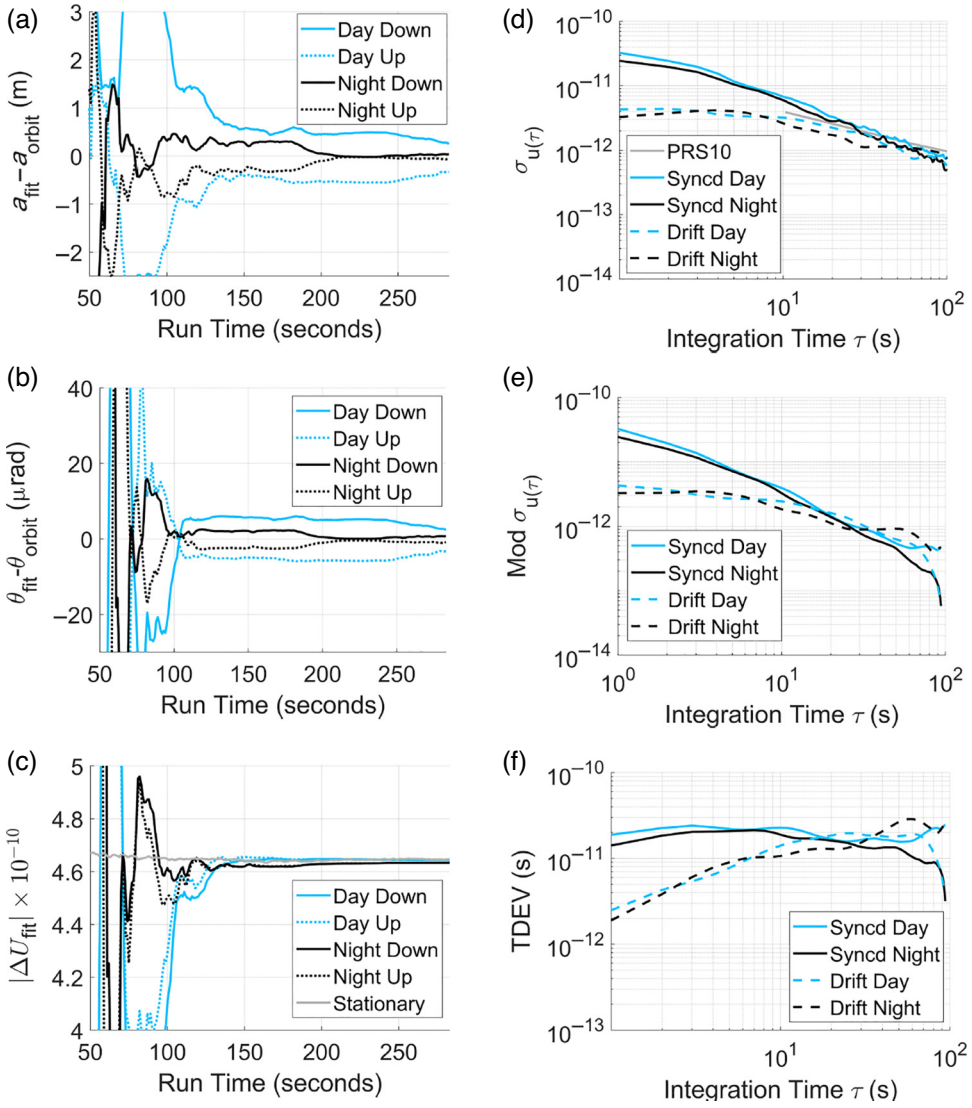

FIG. 8. Plots summarizing the performance of the orbit-tracking algorithm and QTT. (a)–(c) show how the fit algorithm converges to the altitude a, inclination θ_i, and fractional frequency drift ΔU, respectively. (d)–(e) give the Allen deviation, modified Allen deviation, and the time deviation, respectively.

the AO system is driven by a beacon in the downlink direction instead of the point-ahead direction. To emulate this, we remove coincidences in the uplink direction equivalent to an additional 12 dB loss, that is, an uplink-channel loss of ∼36 dB. When the CAR is very low, the QTT algorithm can find an erroneous noise peak instead of the true correlation peak. Therefore, we set a threshold correlation-signal-peak height of 1.8 to veto these measurements and then predict the next clock offset based on the fit of the prior data. Figure 9(a) shows the synchronized clock offset, where the red markers indicate loss of the coincidence signal. As expected, the observed standard deviation of 53 ps is slightly worse than the scenario with 10 dB more signal and no fades [see Fig. 8(c)]. Figure 9(b) shows that the tracking algorithm continues to work despite the signal losses. With only three fades over 283 seconds, it is evident that the QTT algorithm succeeds with approximately 99% probability in this configuration. To corroborate this result, we plot the probability of success given by Eq. (A13) of Ref. [14]. In Fig. 9(c) one can see that given the 2-MHz pair rate and 40% heralding efficiency of the field-experiment biphoton source (see black star), the QTT algorithm is expected to succeed with approximately 99% probability.

In the daytime uplink scenario the extra loss limits the probability of success. However, in a practical quantum network, one would use a source with higher pair rate and higher heralding efficiency to increase the number of coincidences [see Eq. (A4) in Ref. [14]]. In conjunction with adequate spectral filtering, this can increase the attenuation

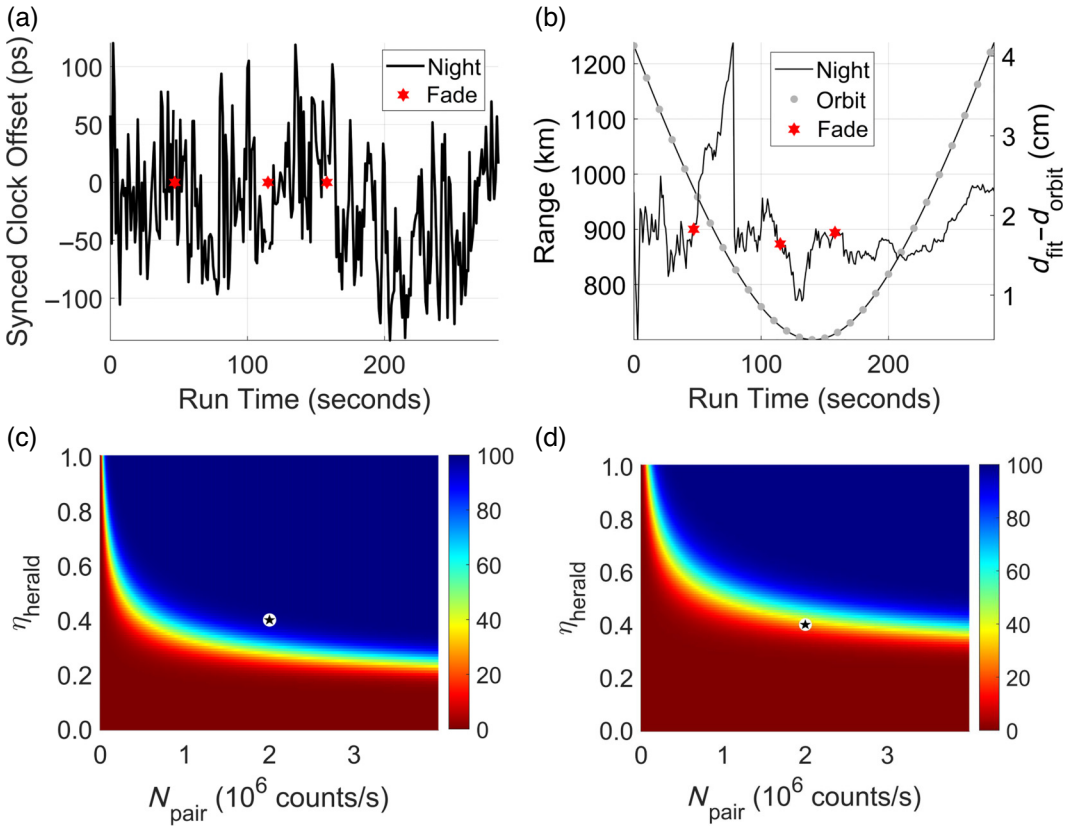

FIG. 9. (a) The synchronized clock offset and (b) the satellite range for the nighttime scenario with 36 dB loss in the uplink channel. The red markers indicate where the signal was temporarily lost. (c),(d) The probability of success as a function of heralding efficiency and pair rate, with black stars giving the approximate performance parameters of the biphoton source used in the field experiment. In (c) we plot the nighttime [1 W/(m^2 sr μm)] uplink condition with 36 dB of channel attenuation. One can see that the QTT algorithm is expected to succeed with about 99% probability. In (d) we plot the daytime [23 W/(m^2 sr μm)] uplink condition with 36 dB of channel attenuation using a 1 nm spectral filter. One can see that a source with heralding efficiency greater than 60% would enable success probability greater than 99%.

tolerance and relax the requirement for the beacon in the point-ahead direction. In Fig. 9(d) we show the probability of success with a 1-nm spectral filter instead of the 10-nm filter used in the field experiment. One can see that narrower spectral filtering in conjunction with modest improvements to the pair rate and heralding efficiency would permit the QTT algorithm to operate reliably in the high-loss and high-noise regime.

[1] M. A. Lombardi, L. M. Nelson, A. N. Novick, and V. S. Zhang, Time and frequency measurements using the global positioning system, Cal Lab: Int. J. Metrol. **8**, 26 (2001).

[2] P. Exertier, E. Samain, N. Martin, C. Courde, M. Laas-Bourez, C. Foussard, and P. Guillemot, Time transfer by laser link: Data analysis and validation to the ps level, Adv. Space Res. **54**, 2371 (2014).

[3] F. R. Giorgetta, W. C. Swann, L. C. Sinclair, E. Baumann, I. Coddington, and N. R. Newbury, Optical two-way time and frequency transfer over free space, Nat. Photon. **7**, 434 (2013).

[4] L. C. Sinclair, W. C. Swann, H. Bergeron, E. Baumann, M. Cermak, I. Coddington, J.-D. Deschênes, F. R. Giorgetta, J. C. Juarez, I. Khader, *et al.* Synchronization of clocks through 12 km of strongly turbulent air over a city, Appl. Phys. Lett. **109**, 151104 (2016).

[5] E. D. Caldwell, J.-D. Deschenes, J. Ellis, W. C. Swann, B. K. Stuhl, H. Bergeron, N. R. Newbury, and L. C. Sinclair, Quantum-limited optical time transfer for future geosynchronous links, Nature **618**, 721 (2023).

[6] I. A. Burenkov, A. Semionov, T. Gerrits, A. Rahmouni, D. Anand, Y.-S. Li-Baboud, O. Slattery, A. Battou, S. V. Polyakov, *et al.* Synchronization and coexistence in quantum networks, Opt. Express **31**, 11431 (2023).

[7] M. Alshowkan, P. G. Evans, B. P. Williams, N. S. V. Rao, C. E. Marvinney, Y.-Y. Pai, B. J. Lawrie, N. A. Peters, and J. M. Lukens, Advanced architectures for high-performance quantum networking, J. Opt. Commun. Netw. **14**, 493 (2022).

[8] K. Schatz, B. Amies-King, S. Albosh, R. Kumar, and M. Lucamarini, in *Quantum Technology: Driving*

Commercialisation of an Enabling Science III, edited by M. J. Padgett, Vol. 12335 (SPIE, Birmingham, United Kingdom, 2023), p. 104.

[9] J. E. Gilligan, E. M. Konitzer, E. Siman-Tov, J. W. Zobel, and E. J. Adles, White rabbit time and frequency transfer over wireless millimeter-wave carriers, IEEE Trans. Ultrason. Ferroelectr. Freq. Control **67**, 1946 (2020).

[10] M. Jamroży, M. Gumiński, G. Kasprowicz, R. Romaniuk, and K. Poźniak, in *Photonics Applications in Astronomy, Communications, Industry, and High-Energy Physics Experiments 2015*, edited by R. S. Romaniuk, Vol. 9662 (SPIE, Wilga, Poland, 2015), p. 357.

[11] A. Valencia, G. Scarcelli, and Y. Shih, Distant clock synchronization using entangled photon pairs, Appl. Phys. Lett. **85**, 2655 (2004).

[12] C. Ho, A. Lamas-Linares, and C. Kurtsiefer, Clock synchronization by remote detection of correlated photon pairs, New J. Phys. **11**, 045011 (2009).

[13] J. Lee, L. Shen, A. Cerè, J. Troupe, A. Lamas-Linares, and C. Kurtsiefer, Symmetrical clock synchronization with time-correlated photon pairs, Appl. Phys. Lett. **114**, 101102 (2019).

[14] R. Lafler and R. N. Lanning, Quantum time transfer: A practical method for lossy and noisy channels, Phys. Rev. Appl. **20**, 024064 (2023).

[15] A. Lamas-Linares and J. Troupe, in *Advances in Photonics of Quantum Computing, Memory, and Communication XI*, edited by Z. U. Hasan, P. R. Hemmer, A. E. Craig, and A. L. Migdall, Vol. 10547 (SPIE, San Francisco, California, 2018), p. 59.

[16] C. Spiess, S. Töpfer, S. Sharma, A. Kržič, M. Cabrejo-Ponce, U. Chandrashekara, N. L. Döll, D. Rieländer, and F. Steinlechner, Clock synchronization with correlated photons, Phys. Rev. Appl. **19**, 054082 (2023).

[17] S. Haldar, I. Agullo, A. J. Brady, A. Lamas-Linares, W. C. Proctor, and J. E. Troupe, Towards global time distribution via satellite-based sources of entangled photons, Phys. Rev. A **107**, 022615 (2023).

[18] S. Haldar, I. Agullo, and J. E. Troupe, Synchronizing clocks via satellites using entangled photons: Effect of relative velocity on precision, Phys. Rev. A **108**, 062613 (2023).

[19] R. Quan, H. Hong, W. Xue, H. Quan, W. Zhao, X. Xiang, Y. Liu, M. Cao, T. Liu, S. Zhang, *et al.* Implementation of field two-way quantum synchronization of distant clocks across a 7 km deployed fiber link, Opt. Express **30**, 10269 (2022).

[20] L. Blanchet, C. Salomon, P. Teyssandier, and P. Wolf, Relativistic theory for time and frequency transfer to order, Astron. Astrophys. **370**, 320 (2001).

[21] M. T. Gruneisen, M. L. Eickhoff, S. C. Newey, K. E. Stoltenberg, J. F. Morris, M. Bareian, M. A. Harris, D. W. Oesch, M. D. Oliker, M. B. Flanagan, *et al.* Adaptive-optics-enabled quantum communication: A technique for daytime space-to-Earth links, Phys. Rev. Appl. **16**, 014067 (2021).

[22] M. D. Oliker and M. T. Gruneisen, in *Quantum Technologies and Quantum Information Science V*, edited by M. T. Gruneisen, M. Dusek, P. M. Alsing, and J. G. Rarity, Vol. 11167 (SPIE, Strasbourg, France, 2019), p. 10.

[23] J. Coakley, Reflectance and albedo, surface, Ency. Atmos. Sci. **12**, 1914 (2003).

[24] W. J. Riley and D. A. Howe, *Handbook of Frequency Stability Analysis* (US Department of Commerce, National Institute of Standards and Technology, Springfield, VA, 2008).

[25] S. Cakaj, B. Kamo, V. Koliçi, and O. Shurdi, The range and horizon plane simulation for ground stations of low Earth orbiting (LEO) satellites, Int. J. Commun. Netw. Syst. Sci. **4**, 585 (2011).

[26] R. K. Tyson, *Principles of Adaptive Optics* (CRC press, Boca Raton, 2015).

[27] N. Martinez, in *Photonics*, edited by M. Brodsky, Vol. 10 (MDPI, Basel, Switzerland, 2023), p. 858.